Journal of Alloys and Compounds 1050 (2026) 185757

Contents lists available at ScienceDirect

Journal of Alloys and Compounds

journal homepage: www.elsevier.com/locate/jalcom

Research article

On the precipitation during age hardening of CoCrFeMnNi with Al and Ti additions

Antoine Hilhorst *, Alvise Miotti Bettanini, Mike Callahan, Pascal J. Jacques

UCLouvain, Institute of Mechanics, Materials and Civil Engineering, IMAP, Place Sainte Barbe 2, Louvain-la-Neuve, 1348, Belgium

ARTICLE INFO

Keywords:
High entropy alloys
Precipitation hardening
Alloy design

ABSTRACT

High entropy alloys (HEAs) based on Co-Cr-Fe-Mn-Ni transition metals with Al and Ti additions constitute a versatile system to generate complex microstructures. In this study, microstructures consisting of a ductile FCC matrix with hard BCC, σ, and fine precipitates are obtained after thermo-mechanical treatments by varying the amounts of Al and Ti, specifically $(CoCrFeMnNi)_{100-x}(Al_2Ti)_x$, $x = 6, 8, 10$. Ageing is performed in the range of 650 to 850 °C up to 160 h. Additionally, the effect of ageing is compared between as-cold-rolled state and after solution treatment. Bulk hardness values ranges from 300 to 600 HV due to the precipitation of a (Cr, Fe, Mn)-rich σ phase and a (Co, Ni, Al, Ti)-rich BCC phase, as characterized by nanoindentation, EBSD, and STEM. A higher content of Al/Ti increases the volume fraction of secondary phases, increasing hardness. During ageing, precipitation occurs in three stages with first the precipitation of a BCC secondary phase, second the concurrent precipitation of σ and BCC phases, and third the formation of needle-like BCC precipitates. $L1_2$ precipitates have not been observed in the range of compositions and heat treatments investigated.

1. Introduction

Precipitation hardening (PH) is an effective method to increase the strength of metallic alloys and has been successfully applied across a broad range of alloys [1–3]. In this study, PH is used to strengthen the equimolar CoCrFeMnNi high entropy alloy (HEA), more widely known as the Cantor alloy. Single phase face-centred cubic (FCC) alloys based on the Co-Cr-Fe-Mn-Ni system have attracted considerable attention in recent years owing to reports of excellent properties with a combination of high ductility and exceptional toughness, even at cryogenic temperatures [4,5]. However, their relatively low yield strength limits their application in structural contexts. Consequently, numerous approaches have been explored to increase its strength, with secondary-phase precipitation emerging as a particularly promising route [6–9].

To strengthen the ductile FCC matrix, strengthening strategies have focused on the controlled precipitation of secondary phases such as disordered or ordered body-centred cubic (BCC A2 or B2) [10–13], sigma (σ) [10,12,14], and $L1_2$ (ordered FCC) [13,15–18] phases. For example, He et al. [19] observed that the addition of 11 at.% of Al to a Cantor alloy causes the precipitation of a BCC phase, increasing the yield strength at room temperature from ~200 MPa to ~800 MPa and increasing the hardness from 170 HV to 525 HV. Similarly, Zhao et al. [20] reported that the addition of Al and Ti in a 2:1 ratio to CoCrFeNi promotes the precipitation of fine (<100 nm) $L1_2$ intermetallic particles, which result in increased hardness and tensile strength of the alloy. Hence, the precipitation of secondary phases seems to bring significant improvement to the yield strength and tensile strength of the material.

Thermodynamic design has been central to tailoring such precipitation. Rieger et al. [21] studied the evolution of the two-phase region, FCC A1 with $L1_2$ precipitates, in the system $(Co_aCr_bFe_cNi_d)_{90}(AlTi)_{10}$ guided by a thermodynamic approach following the CALPHAD method and validated experimentally. They showed the essential role of Al-Co-Ni-Ti in controlling the equilibrium of these phases of interest, with Fe acting as a substituting element to both Co and Ni. Joseph et al. [22] used similar thermodynamic methods to study the effect of Al and Ti additions to the quaternary CoCrFeNi and showed that the combined Al and Ti contents should remain below 18 at.% to favour a dual phase FCC A1 + $L1_2$ microstructure. Kaspar et al. [18] further showed that Al and Ti promote not only $L1_2$ precipitation but also the formation of σ and B2 phases in the system $Co_2CrFeNi_2$. The effect of the simultaneous Al and Ti additions in the quinary CoCrFeMnNi remains relatively unexplored, largely due to the processing challenges caused by Mn [23]. This knowledge gap is significant as Mn complicates precipitation pathways while also influencing phase stability.

A key concern in designing precipitation-hardened alloys is the trade-off between strengthening and ductility. The precipitation of Al-rich BCC or B2 is often accompanied by the stabilization of the brittle σ phase [24], enriched in Fe and Cr, which promotes intergranular

* Corresponding author.
E-mail address: antoine.hilhorst@uclouvain.be (A. Hilhorst).

https://doi.org/10.1016/j.jallcom.2025.185757
Received 1 August 2025; Received in revised form 16 December 2025; Accepted 21 December 2025
Available online 29 December 2025

fracture at particle-matrix interfaces. While σ is classically regarded as detrimental to ductility in conventional alloys, recent studies have shown that the presence of σ phase in Cantor-based HEAs may be less harmful, opening new avenues for microstructural design [6,8,9]. Beyond their role in strengthening, precipitates can also influence high-temperature properties. For instance, fine-scale dispersions may stabilize the microstructure against grain growth [25], improving creep resistance [26,27] or even enabling superplastic deformation [28], as reported in other alloy systems. Such effects highlight that precipitation not only modifies strength and ductility, but can also broaden the range of applications of HEAs. Nonetheless, achieving an optimal balance of properties from a complex microstructure containing $L1_2$ precipitates, BCC, and σ phases remains a challenge.

Despite rapid advances, precipitation hardening in HEAs is still at an early stage of development. PH HEAs showed promising results, rivalling or exceeding the strength-ductility combinations of commercial superalloys [29,30] but their precipitation pathways are not yet fully understood. Importantly, most prior studies have focused on ageing following homogenization or solution heat treatment, i.e. after recrystallization. However, pre-deformation (e.g. cold rolling) is well known to significantly change the precipitation behaviour in conventional alloys such as Ni-rich stainless steels [31] and Ni superalloys [32] to strongly influence nucleation and growth of precipitates, thereby altering both phase selection and distribution. This critical aspect remains not yet well understood in PH HEAs, particularly in Cantor-based systems with concurrent Al and Ti additions [33,34].

In this work, we investigate the precipitation hardening behaviour of the equimolar CoCrFeMnNi HEA with additions of Al (up to 7 at.%) and Ti (up to 3.5 at.%) as a function of ageing temperature (650 °C to 850 °C) and time (up to 160 h) to capture both the precipitation at the early stages as well as the near-equilibrium state with potential late-stage transformations such as coarsening or phase ordering. The hardness is characterized by micro- and nano-indentation. Microstructural evolution during ageing is characterized using scanning and transmission electron microscopy, revealing a complex multiphase structure comprising BCC and σ phases in the FCC matrix. The morphology, crystallography, and composition of the different phases are examined. Furthermore, the PH effect is compared between the as-cold-rolled and solution-treated conditions. The experimental findings are interpreted from a thermodynamic perspective, comparing experimental results to CALPHAD predictions.

2. Materials and methods

Pure elements (>99.9%) were arc-melted to obtain a master ingot of equiatomic CoCrFeMnNi. Three alloys with slightly different contents of Al and Ti were manufactured starting from the equimolar Cantor alloy: $(CoCrFeMnNi)_{94}(Al_2Ti)_6$, $(CoCrFeMnNi)_{92}(Al_2Ti)_8$, and $(CoCrFeMnNi)_{90}(Al_2Ti)_{10}$, which will be referred to as Al_2Ti-6, Al_2Ti-8, and Al_2Ti-10, respectively. The nominal and actual chemical compositions of the three alloys measured by inductively coupled plasma (ICP) mass spectrometry, using a ICP-OES 5100 from Agilent Technologies, are reported in Table 1. After casting, the ingots were homogenized at 1100 °C for 4 h. Then, they were hot rolled from 10 to 5 mm at 1100 °C (50% reduction) and cold rolled down to a final thickness of 2 mm (60% reduction). Samples in this state will be referred as "as-rolled (AR)". One series of each of the three compositions was solution heat treated at 1100 °C for 45 min in order to recrystallize the cold-rolled microstructures. Samples in this state will be referred as "solution treated (ST)". Finally, small samples (2 mm × 2 mm × 10 mm) in the AR and ST states were aged for at least 100 h at 650 °C, 750 °C, and 850 °C, with selected conditions extended to 160 h.

The composition and heat treatments employed in this study were first selected based on prior reports of alloys with similar compositions [15,20,35], where such conditions were shown to promote the formation of an FCC matrix with precipitation strengthening. To verify the suitability of these conditions for the present alloy systems, thermodynamic simulations were performed using Thermo-Calc [36] with the TCHEA5 database. The simulations confirmed that the chosen heat treatments would yield the desired microstructural constituents, namely an FCC matrix with σ, BCC precipitates, and with either a significant, a moderate, or no precipitation of $L1_2$ phase at 650, 750, and 850 °C, respectively.

Table 1
Chemical compositions of $(CoCrFeMnNi)_{94}(Al_2Ti)_6$ (Al_2Ti-6), $(CoCrFeMnNi)_{92}(Al_2Ti)_8$ (Al_2Ti-8), and $(CoCrFeMnNi)_{90}(Al_2Ti)_{10}$ (Al_2Ti-10) alloys. Actual compositions are measured by ICP with a standard deviation of 0.15 at.%. Unless stated otherwise, all the compositions are reported in at.%.

	Co	Cr	Fe	Mn	Ni	Al	Ti	[at.%]
Al_2Ti-6	18.8	18.8	18.8	18.8	18.8	4	2	Nominal
	18.3	19.3	19.0	18.6	18.7	4.5	1.6	Actual
Al_2Ti-8	18.4	18.4	18.4	18.4	18.4	5.3	2.6	Nominal
	18.3	17.9	18.0	19.1	18.0	5.9	2.7	Actual
Al_2Ti-10	18.0	18.0	18.0	18.0	18.0	6.7	3.3	Nominal
	18.2	18.2	17.9	17.9	18.1	6.5	3.2	Actual

After heat treatments, samples were mounted and polished following standard metallography practices. The last steps consisted in polishing with a 1 μm diamond paste followed by alumina oxide particles in suspension (OPS) polishing. These samples were then characterized with scanning electron microscopy (SEM), a ULTRA55 from Zeiss, using back-scatter electrons (BSE) to produce images based on the strong chemical heterogeneity of the different phases. Unless stated otherwise, the micrographs were acquired with the SEM operating at 15 kV using a 60 μm aperture. The phase volume fractions were extracted from series of SEM micrographs using image analysis, with an example of the method provided in the Supplementary Materials (Figure S1). Phase compositions were characterized using energy dispersive spectroscopy (SEM-EDS) using Bruker XFlash 5010 with a detector size of 30 mm^2 mounted with a Be window. Qualitative EDS maps were also obtained for different conditions to improve phase identification by image analysis, see the Supplementary Materials for details (Figure S2). The crystallography of the different phases was identified by electron back-scattered diffraction (EBSD) using a SEM SUPRA55 from Zeiss operating at 30 kV equipped with a Symmetry detector from Oxford Instruments. Finally, the micro-hardness of all the characterized microstructures was tested with a micro-indenter using a 200 g mass. One transmission electron microscopy (TEM) sample was prepared by focused-ion beam (FIB), a Helios Nanolab from FEI, for Al_2Ti-10 annealed at 650 °C for 32 h. The surface of the sample was coated by focused-ion beam induced deposition with a thick platinum layer to prevent damage. The lamella was first thinned using a 30 kV Ga beam, before a final cleaning step at 8 kV to limit damages and reduce the superficial amorphized layer. STEM micrographs were obtained at 200 kV. The software PTCLab [37] has been used to simulate TEM diffraction patterns.

3. Results

The microstructure after rolling is dual phase with a heavily deformed face centred cubic (FCC) matrix and a body-centred cubic (BCC) second-phase, forming large round precipitates at the FCC grain boundaries. Based on thermodynamic calculations, the volume fraction of B2 at 1150 °C is predicted as 0, 6, and 12% using the actual compositions (Table 1) for Al_2Ti-6, Al_2Ti-8, and Al_2Ti-10, respectively. The solution treatment (ST) at 1150 °C recrystallizes the FCC phase and only partly dissolves the BCC phase, even in the case of Al_2Ti-6. The microstructures obtained after rolling are shown in Supplementary Materials (Figures S3a–c).

Fig. 1 shows the microstructure evolution with ageing at 650 °C for Al_2Ti-6, the smallest addition of Al and Ti investigated, comparing the

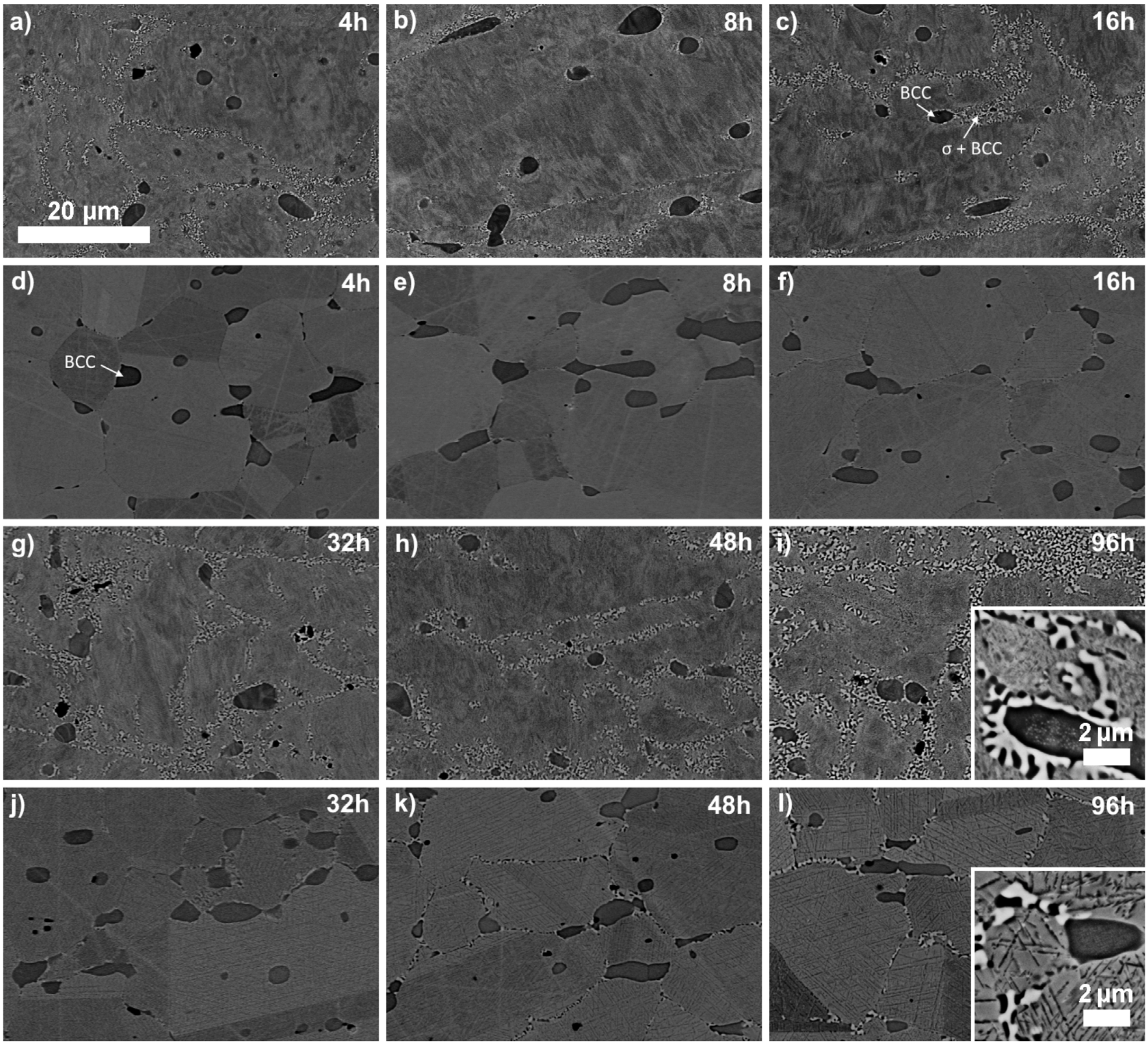

Fig. 1. SEM-BSE micrographs of Al_2Ti-6 after different ageing time from 4 to 96 h at 650 °C, either directly after rolling (a–c, g–i) or after a solution treatment at 1150 °C for 4 h (d–f, j–l). Higher resolution insets are shown for Al_2Ti-6 aged at 650 °C for 96 h after rolling as well as after solution treatment.

effect of a solution heat treatment before ageing, or the lack thereof. At this temperature, precipitation is preferred as the dominant pathway compared to recrystallization. In the case of ST samples, initially single-phase FCC, the BCC second-phase is already observed after ageing for 1 h. Three other precipitation phenomena occur with further ageing, observed in aged as-rolled (AR) and aged ST samples. First, two phases precipitate simultaneously, decorating grain boundaries, appearing lighter and darker than the FCC matrix with SEM-BSE imaging, respectively. The crystallography is identified by EBSD, as discussed later, as σ and BCC phases for the light and dark phases, respectively. It is worth noting that ordering cannot be assessed by EBSD and at this stage, the distinction will not be made between disordered BCC and ordered BCC e.g. B2 or $L2_1$, nor between disordered FCC and ordered FCC, e.g. $L1_2$. In the case of AR samples, the σ and BCC precipitation is already observed after ageing for 1 h for all temperatures. In the case of ST samples, precipitation starts between 8 and 16 h of ageing (Fig. 1f) at 650 °C. At 850 °C, σ phase is already observed after 1 h of ageing (Fig. 4). A secondary precipitation is observed in the form of dark needles (BCC) in the FCC matrix. These needles are larger in ST samples, see inset of Fig. 1l. Finally, precipitation occurs in the BCC second-phase in the form of fine white globules (see inset of Fig. 1i). Additional micrographs with a higher magnification are shown in Supplementary Materials for Al_2Ti-6 after ageing at 850 °C for 1, 24, 40, and 96 h (Figures S4–S7).

In order to demonstrate the effect of the ageing temperature, Fig. 2 shows the microstructures of AR and ST samples of Al_2Ti-6 aged for 32 h at 850 °C. When compared with the microstructures obtained at 650 °C in Fig. 1, the same phases can be identified, albeit coarser. The major difference is the recrystallization of the FCC matrix in AR samples.

Increasing the Al and Ti contents affects the phase volume fractions of σ, BCC, and FCC phases. Fig. 3 shows the microstructure of Al_2Ti-10 aged 32 h at 650 and 850 °C for AR and ST samples, respectively. Similar microstructures to the ones previously shown in Figs. 1g-j and Fig. 2 are obtained. Greater amounts of σ and BCC phases are observed for Al_2Ti-10 for all heat treatments.

Fig. 4 shows EBSD band contrast maps with FCC, BCC, and σ phases overlaid in colour for Al_2Ti-6 aged at 850 °C for short and long times in the case of AR and ST samples. Only partial recrystallization occurs at 850 °C in AR samples, as several grains show residual deformation, see the inverse pole map in the inset of Fig. 4b and Figure S8, the kernel average misorientation maps.

Fig. 5 shows STEM characterization obtained for a Al_2Ti-10 sample after ST and aged at 650 °C for 32 h. The FIB lamella was extracted

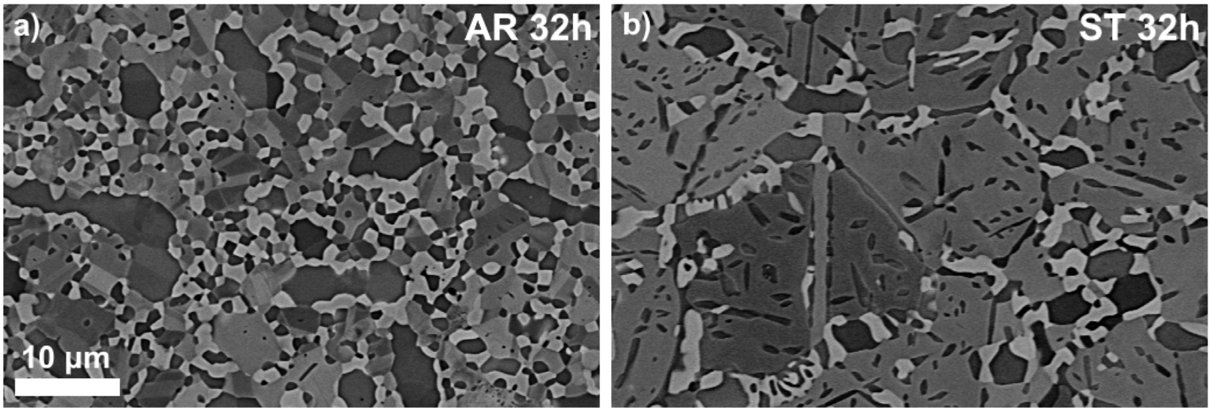

Fig. 2. SEM-BSE micrographs of Al_2Ti-6 after ageing at 850 °C for 32 h (a) directly after rolling (AR) and (b) after solution treatment (ST).

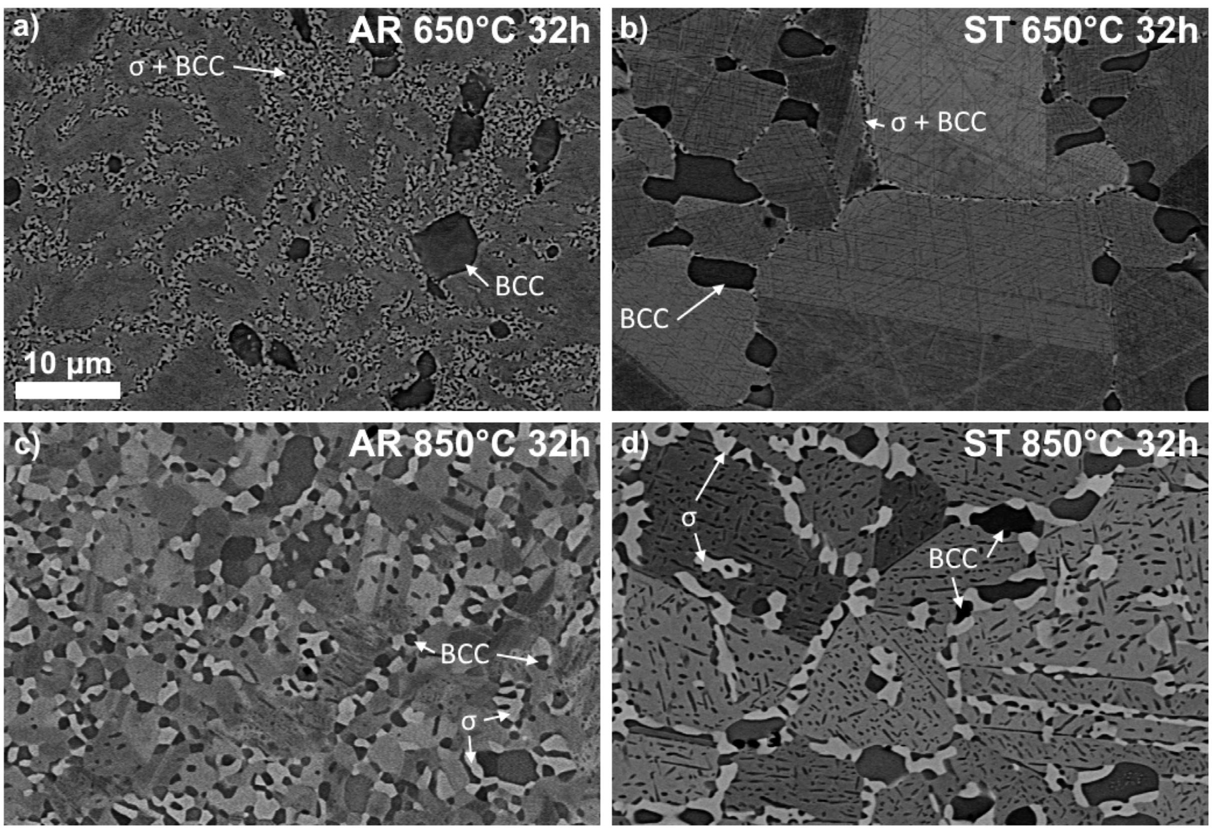

Fig. 3. SEM-BSE micrographs of Al_2Ti-10 after ageing for 32 h at 650 °C (a–b) and 850 °C (c–d), directly after rolling and (a–c), after solution heat treatment (b–d).

from a FCC grain containing small dark precipitates, away from the grain boundaries (containing σ and BCC phases). At low magnification (Fig. 5a), precipitates organized in needles are observed in a matrix. At higher magnification (Fig. 5b), defects can be observed within the matrix, which are characteristic of FIB-induced damage [38]. By EDS (Figs. 5f–l), two regions can be observed in the precipitates, as Al, Co, Mn, Ni, and Ti segregate from Cr. Fe is mainly present in the matrix, Al and Ti are mostly present in the precipitates. Table 2 gives the compositions of areas c, d, and e as highlighted in Fig. 5b, measured by TEM-EDS. From the diffraction patterns (Figs. 5c–e), the structure of the matrix was identified as FCC and the structure of the precipitates was identified as BCC. No difference in lattice parameter could be observed between the Cr-rich ($p1$) and the Cr and Fe depleted ($p2$) regions within the precipitates. Measuring the planar interdistance, the lattice parameters of the FCC and BCC phases are 0.361 and 0.291 nm, respectively. Zone axes [110] and [111] could be confidently observed in diffraction for the matrix and precipitates, respectively. Areas where both the matrix and precipitates diffracted simultaneously were observed but no apparent orientation relationship exists between both phases. In order to discriminate between disordered and ordered BCC, other zones axes have been investigated. The diffraction patterns obtained in these conditions are less sharp due to the large tilt angles involved. Fig. 6(a, b) shows superlattice reflections associated to $L2_1$ in the case of the diffraction of Al-, Co-, Mn-, Ni-rich precipitates ($p2$ in Table 2), whereas Cr-rich precipitates are disordered BCC A2, (Fig. 6c). It is worth noting that the lack of additional reflections in the case of the diffraction of FCC with a zone axis of [110] (Fig. 5c) or [125] (Fig. 6d) indicates the absence of $L1_2$ precipitates within the matrix in the present sample.

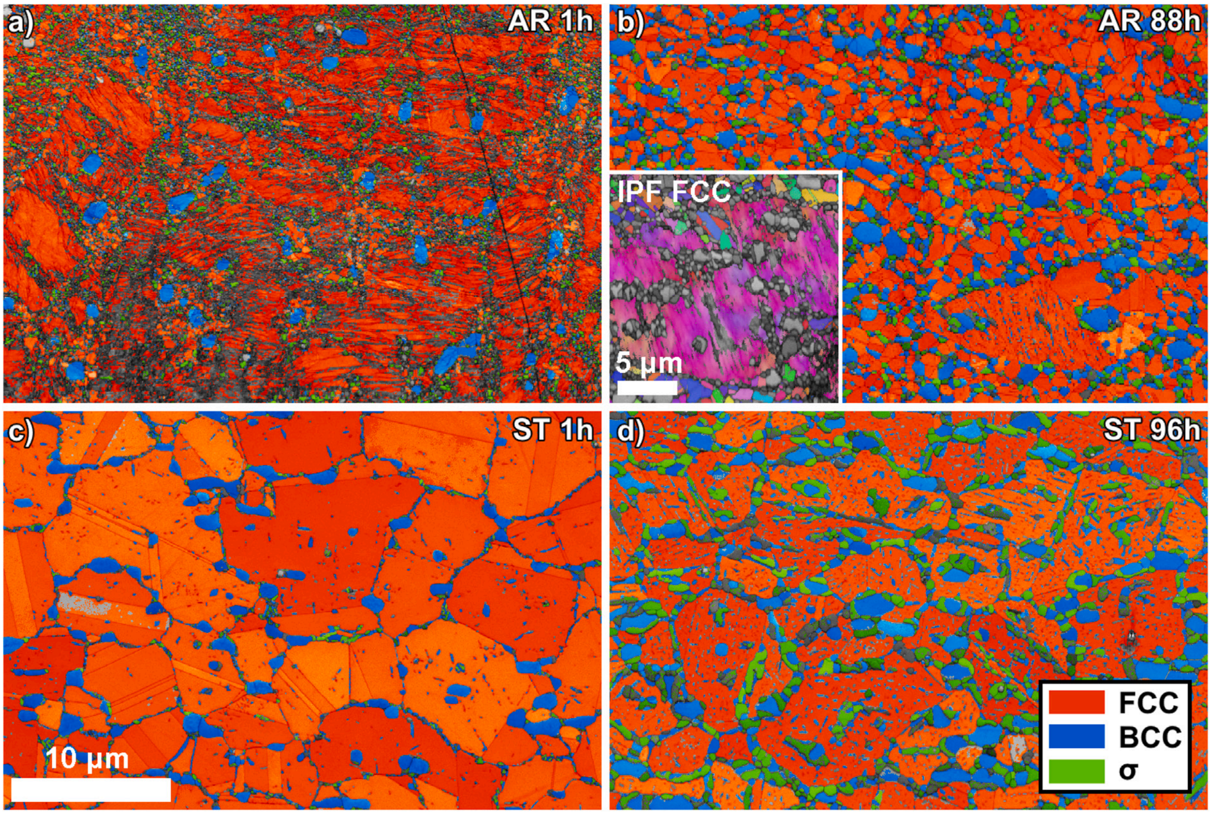

Fig. 4. EBSD band contrast maps with FCC, BCC, and σ phase overlaid in red, blue, and green, respectively for as-rolled Al_2Ti-6 aged at 850 °C (a) for 1 h, and (b) 88 h, and for solution treated Al_2Ti-6 aged (c) for 1 h, and (d) 96 h. The inset in (b) shows the inverse pole figure (IPF) map for FCC for an unrecrystallized region.

Table 2
Compositions in at.% of the matrix and precipitates (*p*1 and *p*2), corresponding to areas c, d, and e, respectively, in Fig. 5b measured by TEM-EDS. Values are given within ±1 at.%.

	Al	Co	Cr	Fe	Mn	Ni	Ti
Matrix	0	17	21	26	20	14	2
*p*1	3	6	69	6	8	6	2
*p*2	19	23	3	4	16	27	8

Fig. 7 shows the evolution of the micro-hardness of the three alloys during ageing at 650, 750, and 850 °C, respectively. After ST and before ageing, the average hardness is similar across samples with different (Al_2Ti) content and equal to 199 ± 8 HV. Ageing increases the hardness for all Al and Ti contents. After 2 h at 850 °C, the average hardness reaches 325 ± 8 HV. On the other hand, the increase in hardness is less steep for ageing at 650 °C with 270 ± 6 HV after 2 h. For longer ageing time, the hardness of the alloys treated at 650 °C increases to approximately 450 HV, while for ageing at 850 °C, the peak hardness is only 350 HV. In the case of AR samples, ageing further than 4 h does not increase hardness. In the case of ST samples, the hardness reaches a maximum after 24 h for Al_2Ti-8 and Al_2Ti-10, and after 64 h for Al_2Ti-6.

In order to understand the complex relationship between the hardness and the microstructure, local hardness has been measured by nanoindentation. However, a clear correlation between each phase and the hardness is difficult to obtain due to the small number of indents (100) relative to the fine and complex nature of the observed microstructures. Fig. 8 shows the histograms of hardness values obtained for each nanoindentation map with the corresponding SEM micrograph given for Al_2Ti-6 aged at 850 °C for a short and a long time in the case of AR and ST samples, respectively, with values ranging from 2 to 16 GPa. From the qualitative observations of the histograms, combined with the direct observations of the indents position by SEM, ranges of hardness values can be attributed to each phase, as identified by SEM-EBSD. Relatively low hardness values ranging from 4 to 8 GPa can be attributed to the FCC matrix. It is worth noting that in the case of ST samples, the FCC matrix (with BCC precipitates) presents values in the range of 4 to 6 GPa. In the case of AR samples, after ageing for 2 h, the matrix presents a larger average hardness of 6 GPa, while, after ageing for 96 h, recrystallized regions present values of approximately 5 GPa and un-recrystallized presents values of approximately 6 to 7 GPa. Hardness values of 8 to 10 GPa are attributed to the BCC secondary phase. The largest recorded hardness values are attributed to σ phase.

4. Discussion

The Cantor system Co–Cr–Fe–Mn–Ni is prone to σ phase precipitation during low temperature annealing [39]. Al additions favour the formation of an ordered BCC B2 phase [13] but also the formation of σ phase [24]. Ti additions can bring the precipitation of Ni_3Ti. The combination of Al and Ti additions favours the formation of coherent ordered FCC $L1_2$ precipitates [18,40,41]. Fig. 9 shows the evolution with temperature of the volume fractions of the σ phase, the ordered B2 secondary phase, as well as the $L1_2$ phase, with the amount of FCC omitted for clarity, at equilibrium for the three alloys investigated, as predicted by the Thermo-Calc software. Increasing the (Al_2Ti) content increases the volume fraction at equilibrium of σ, BCC B2, and FCC $L1_2$ across the range of investigated ageing temperatures. Table 3 lists CALPHAD predictions of the chemical compositions of the phases at 650 °C and 850 °C for Al_2Ti-8. The element partitioning shows that the B2 phase is Al, Co, Mn, and Ni rich; the FCC $L1_2$ is Co, Ni, and Ti rich with a moderate amount of Al; and the σ phase is Co, Cr, Fe,

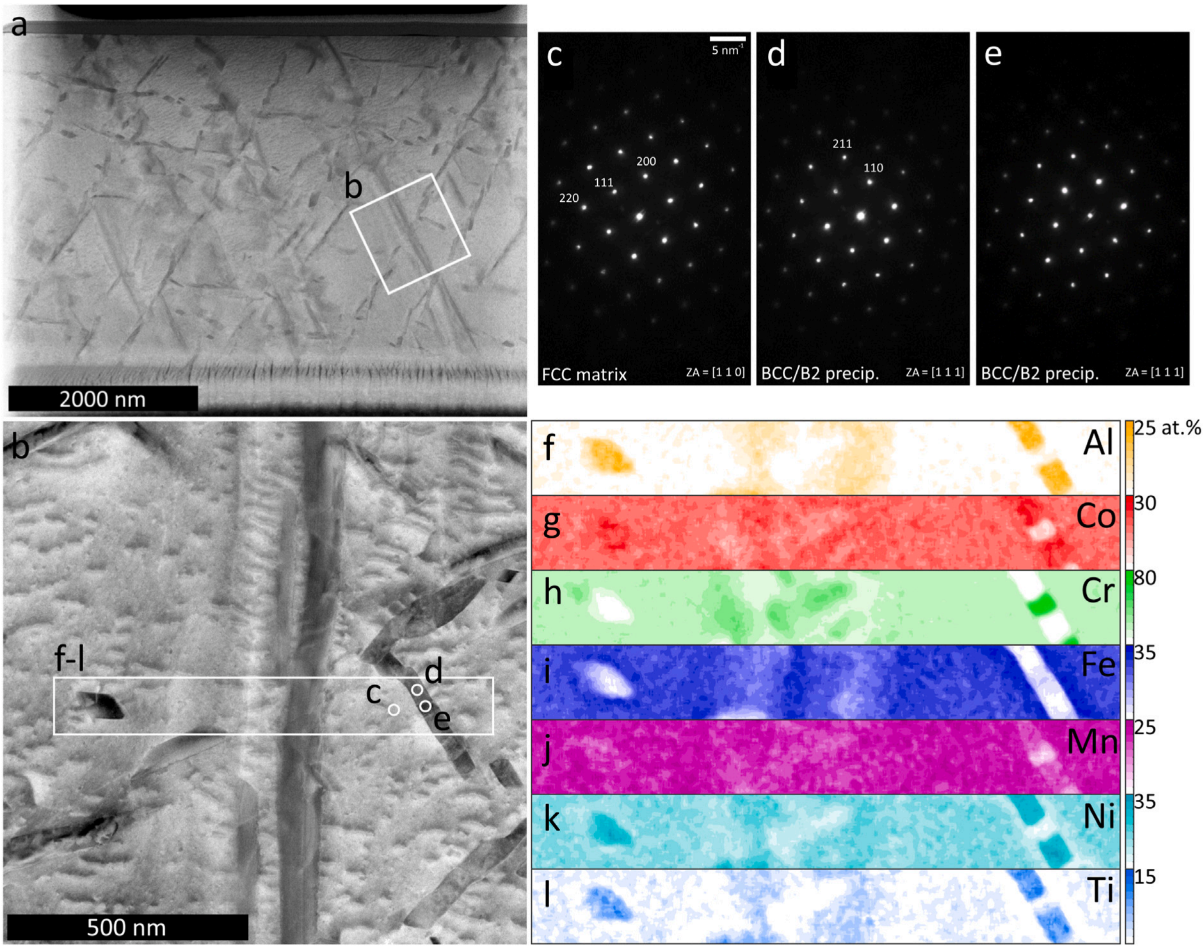

Fig. 5. (a) Low magnification STEM micrograph of a ST Al_2Ti-10 sample aged at 650 °C for 32 h. (b) Higher magnification of the area highlighted in (a). (c, d, e) Diffraction patterns associated to the areas indicated in (b). (f–l) STEM EDS for elements Al, Co, Cr, Fe, Mn, Ni, Ti for the rectangular area highlighted in (b).

and Mn rich. Assuming B2 precipitate first at grain boundaries, the local composition of the surrounding matrix will be Cr and Fe-rich, and poor in Al and Ti, which would favour σ phase formation. Inversely, assuming σ precipitates first would result in B2 precipitation. This explains the concurrent precipitation of σ and BCC, as observed in Figs. 1–4. Adjacent σ and B2 precipitates share an orientation relationship, as it has been observed in Cantor-type HEAs, e.g. [42,43].

The CALPHAD predictions significantly overestimate the amount of secondary phases at 650 °C, especially the amount of σ phase, see Fig. 9. These discrepancies are unlikely to result from sluggish diffusion, which is often assumed in HEAs, as it is not a pronounced effect in Co–Cr–Fe–Mn–Ni systems [44,45]. The thermodynamic calculations offer better predictions for 850 °C. Another important observation is that phase fractions are different between AR and ST states. Residual strain from rolling provides faster diffusion paths as well as stored energy, favouring the precipitation of secondary phases [31].

By SEM image analysis and EDS mapping, the phase fractions can be measured for the different samples, although this quantification is only reliable in conditions where sufficient phase contrast can be achieved. For EDS maps, features smaller than 1 μm cannot be resolved, but the maps can still help distinguish phases in SEM micrographs where phase contrast is insufficient. Fig. 10 shows the evolution of the BCC and σ volume fractions as a function of ageing time for AR and ST conditions. At 650 °C, there is a significant difference in the precipitation behaviours of BCC and σ phases. On the one hand, σ, which is barely present in the ST samples (less than 5% after 96 h), accounts for more than 10% of the microstructures in AR samples after

Table 3
The equilibrium phases and the compositions of the phases stable at 650 °C and 850 °C for Al_2Ti-8. υ_f is the phase molar fraction in mol.% and compositions are reported in at.%. The bold typeface illustrates the first and second richer elements in each phase.

650 °C	υ_f	Co	Cr	Fe	Mn	Ni	Al	Ti
σ	53.5	15.9	**30.6**	**28.4**	21.9	3.2	/	/
BCC B2	26.2	**21.8**	4.2	7.7	20.5	**28.4**	16.1	1.2
FCC A1	6.3	**30.6**	14.4	15.3	16.7	**22.0**	0.3	0.6
FCC $L1_2$	14.0	16.1	0.3	1.7	1.6	**56.1**	7.7	**16.5**
$A1+L1_2$	20.3	**20.6**	4.7	5.9	6.3	**45.5**	5.4	11.6
850 °C	υ_f	Co	Cr	Fe	Mn	Ni	Al	Ti
σ	33.6	13.0	**33.2**	**28.9**	20.5	4.4	/	/
BCC B2	27.6	**18.9**	4.9	5.7	15.7	**30.7**	17.3	6.8
FCC A1	38.8	**22.7**	15.2	18.3	18.6	**21.8**	1.4	2.0

96 h. Moreover, the σ phase appears during the early stages of ageing in AR samples, whereas in ST samples it is only observed after ageing for more than 16 h. On the other hand, BCC phase precipitates together with σ in AR samples, but it also forms as fine needles in ST samples when aged longer than 24 h, as shown in Figs. 1g–l and Figs. 3a, b. At 850 °C, the differences in BCC and σ volume fractions are less pronounced but the precipitation kinetics are significantly slower in ST samples. It is worth noting that needle-like BCC precipitates are also observed in ST samples aged at 850 °C, although they are coarser than those formed at 650 °C, as observed in Fig. 4d.

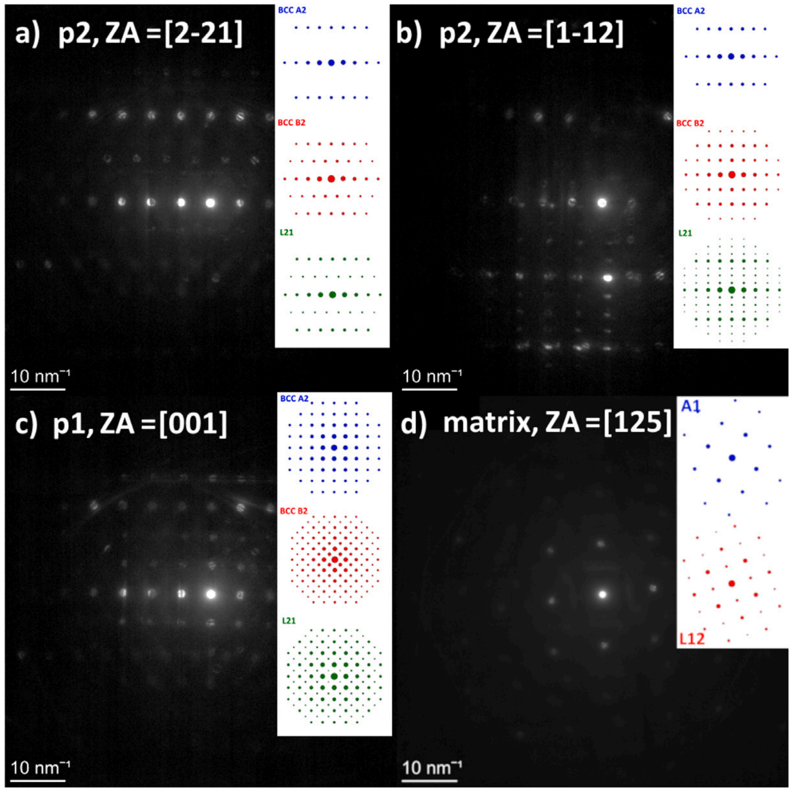

Fig. 6. STEM microprobe diffraction of Al_2Ti-10 sample after ST and aged at 650 °C for 32 h. Diffraction patterns associated to (a, b) Al-, Co-, Mn-, Ni-rich precipitates *p*2, (c) Cr-rich precipitates *p*1, and (d) the disordered FCC matrix.

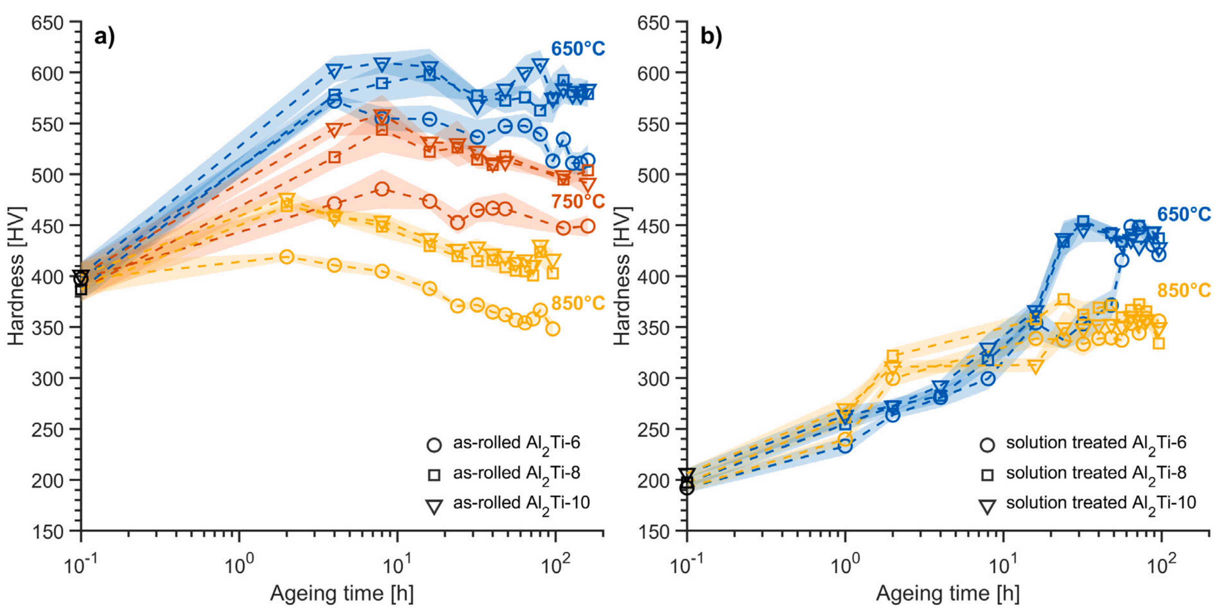

Fig. 7. Evolution of the Vickers hardness of aged (a) as-rolled and (b) solution treated Al_2Ti-6, Al_2Ti-8, Al_2Ti-10 during ageing at 650 °C, 750 °C and 850 °C up to 160 h. Standard error is represented by the shaded areas.

This microstructural evolution explains the distinct hardening behaviours of AR and ST samples with ageing, as schematically shown in Fig. 11. The co-precipitation of fine σ and BCC precipitates in a partially recrystallized matrix is responsible for the higher hardness of AR samples aged at 650 °C, whereas the larger fraction of recrystallized regions and the coarser precipitates in AR samples aged at 850 °C lead to lower hardness. In ST samples, the hardness remains very low for short ageing time due to the fully recrystallized microstructure containing large FCC grains. With further ageing at 850 °C, the increasing hardening can be attributed to the co-precipitation of σ and BCC. Finally, the presence of very fine needles in the FCC matrix explains why ST samples aged at 650 °C exhibit higher hardness than those aged at 850 °C after ageing longer than 32 h, despite having a lower total precipitate fraction.

There has been no clear evidence of $L1_2$ precipitation. It should be noted that EBSD cannot distinguish ordering, so disordered BCC (A2) and ordered B2 or FCC and $L1_2$ phases may be indistinguishable. In

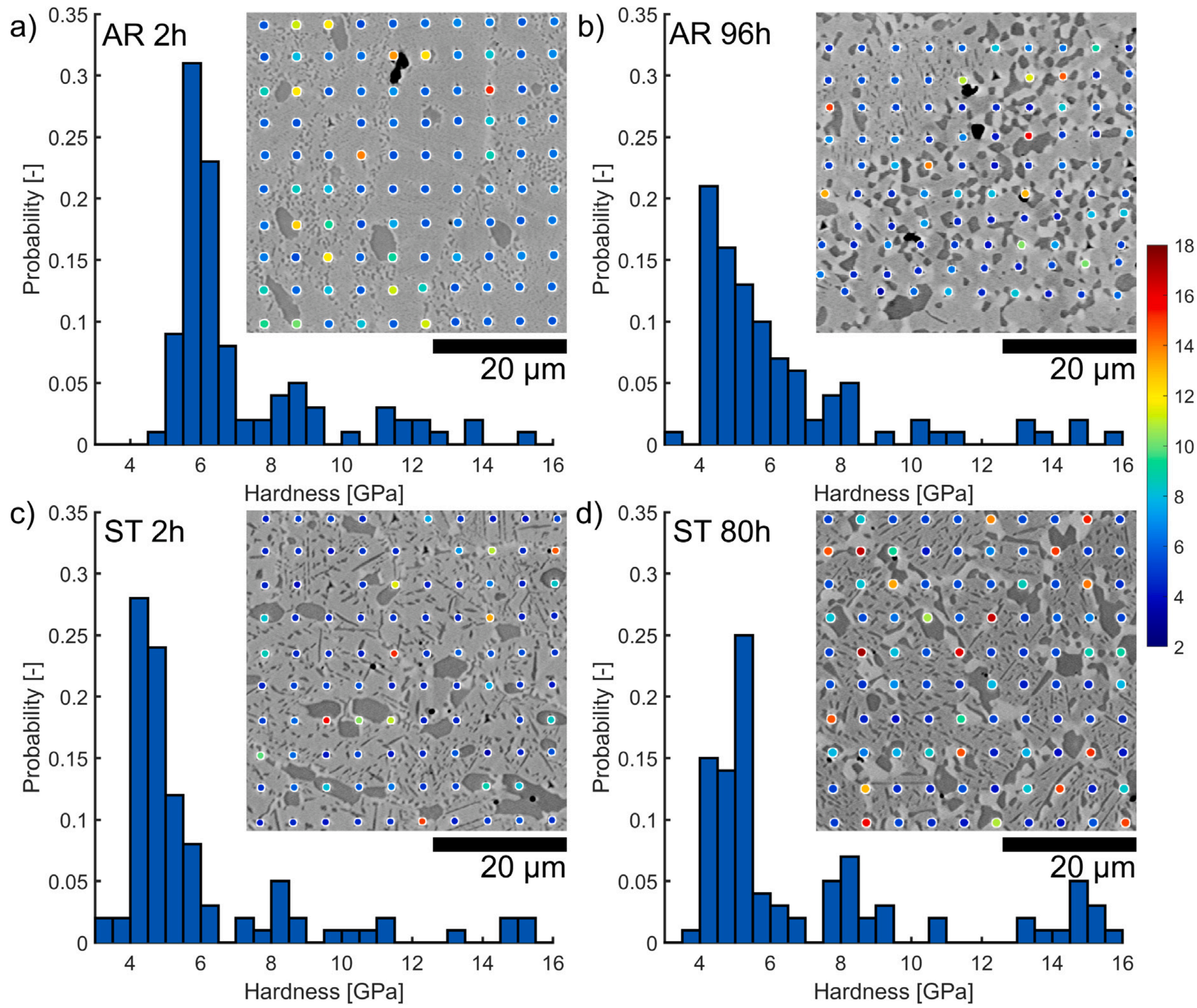

Fig. 8. Normalized histogram of local hardness for 10 by 10 indents nanoindentation maps for Al_2Ti-6 aged at 850 °C (a) for 2 h, and (b) 96 h directly after rolling (AR), and (c) for 1 h, and (d) 80 h after solution treatment (ST). A SEM-BSE micrograph with markers coloured as a function of the hardness is shown in each case.

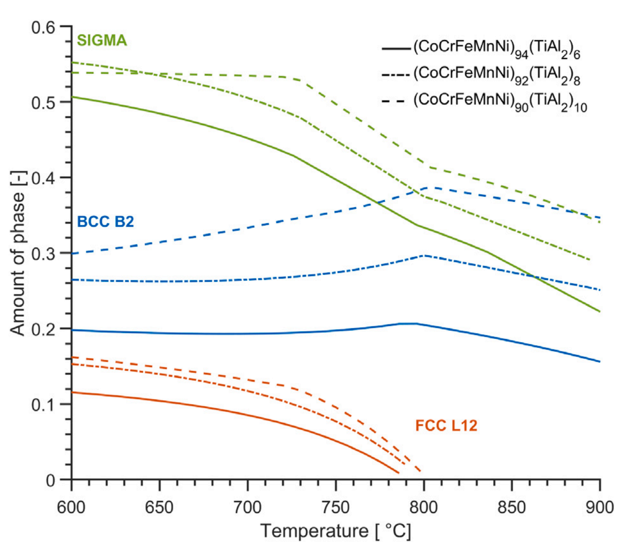

Fig. 9. Evolution of the molar fraction of phases with temperature for Al_2Ti-6, Al_2Ti-8, and Al_2Ti-10 as predicted by Thermo-Calc. The amount of disordered FCC (A1) phase is not shown for clarity.

addition, very fine $L1_2$ precipitates may fall below the detection limits of SEM-EDS and even conventional TEM [46,47]. The absence of $L1_2$ precipitates is likely due to several factors: the nucleation kinetics may be slow under the applied ageing conditions, and early precipitation of BCC/σ could deplete solutes required for $L1_2$ formation. Such mechanism has been observed by Niu et al. [48] in $Al_x(Cr_{35-x}Fe_{30}Ni_{35})$ alloys. The co-precipitation of σ and BCC phases has been observed in HEAs by other authors. Chen et al. [49] observed the co-precipitation of $L2_1$ and BCC phases in $Fe_{40}Ni_{30}Cr_{20}Al_5Ti_5$. Yang et al. [50] studied $(CoCrFeMnNi)_{95.2}(Al_2Ti)_{4.8}$ with annealing from 750 to 1000 °C for 1 h, showing the co-precipitation of B2 and σ phases. Finally, it is known that CALPHAD predictions tend to overestimate $L1_2$ stability in HEAs [13,21,51].

Consistent with these considerations, TEM characterization of Al_2Ti-10 aged at 650 °C showed no $L1_2$, despite being the conditions most likely to precipitate $L1_2$ according to CALPHAD predictions. The fine white precipitates observed in Fig. 1i inset are unlikely to correspond to the $L1_2$ phase as it typically precipitates from FCC A1 and not A2/B2 [16,21]. In Ni-based superalloys, similar small precipitates that are formed inside a secondary BCC phase have been identified as B2 [52].

Although tensile properties were not investigated here, microstructural analysis indicates that precipitate distribution strongly influences ductility. Precipitation at grain boundaries is typically associated with reduced ductility and potential intergranular fracture [53]. However,

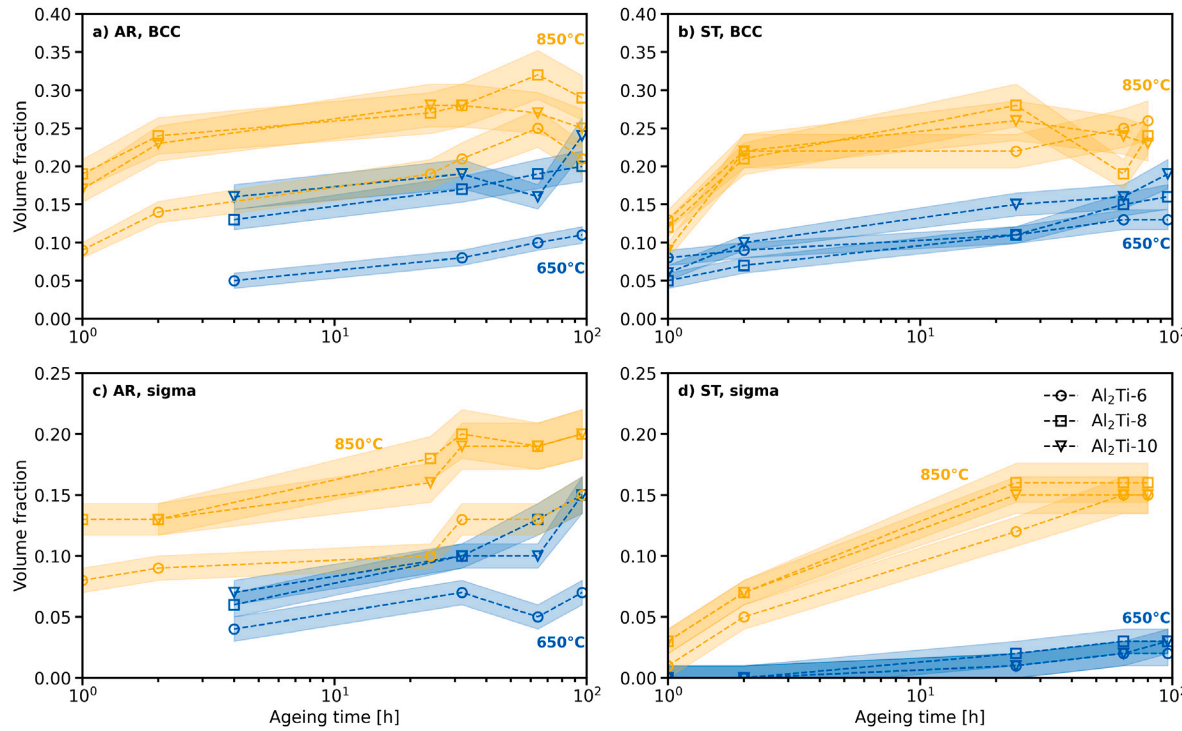

Fig. 10. Evolution of the volume fractions of BCC and σ phases with temperature for Al_2Ti-6, Al_2Ti-8, and Al_2Ti-10 as measured by image analysis of SEM-BSE micrographs.

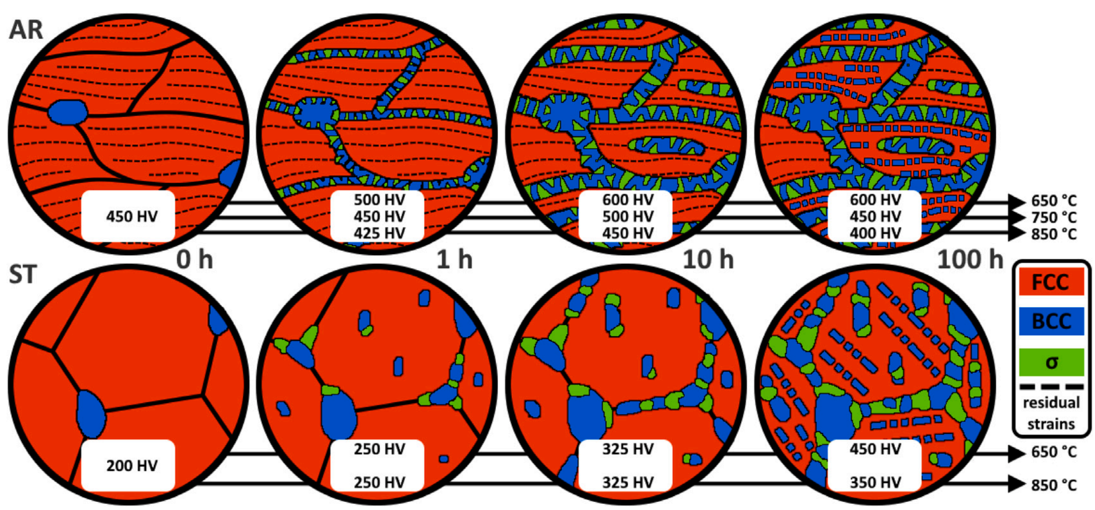

Fig. 11. Schematic evolution of the microstructures with ageing for AR and ST samples.

recent studies have shown promising results for heterogeneous precipitations in medium or high entropy alloys. Park et al. [54] studied heterogeneous precipitation in $Ni_35(FeCoCr)_53Al_7Ti_5$ and showed that, even with significant precipitation of B2 at grain boundaries, the uniform elongation remained at >20% but with a 400-MPa increase of the ultimate tensile strength. Kim at al. [55] showed that a Fe-rich Fe–Ni–Cr–Al–Ti–Nb–C alloy remained ductile but with a significant increase in strength thanks to the heterogeneous precipitation of $L1_2$ at grain boundaries. It is worth noting that precipitates are finer and better distributed in AR samples compared to the large grains observed in the case of ST samples which are decorated with σ and BCC precipitates, suggesting that AR samples may retain better ductility. Even in cases where ductility is reduced, high-hardness alloys remain attractive for specialized wear-resistant coating applications [13].

The σ phase is well known in stainless steels and is typically detrimental to mechanical properties due to embrittlement [56,57]. However, in Cr-rich HEAs, σ is frequently observed [58,59], and several studies indicate that σ phase can contribute to strength while having a limited effect on ductility [9,49,60]. For instance, Cho et al. [61] found that $Co_{20}Cr_{25}Fe_{20}Mn_{20}Ni_{15}$ alloys with up to 15 vol.% of σ phase still exhibited high uniform strain (50%). Similarly, Liu et al. [8] also showed that a triplex $Al_{0.3}$CoCrFeNi (FCC matrix, B2 14 vol.%, σ 5 vol.%) possessed excellent fatigue resistance while maintaining good strength and ductility. Together, these studies highlight the potential of complex multiphase microstrucures with FCC matrices that retain high strain-hardening capacity.

The role of manganese is limited in controlling precipitation in Cantor-based systems, as similar microstructures have been reported in Al–Co–Cr–Fe–Ni–Ti alloys. Nevertheless, Mn can complicate processing through oxide formation [62,63], although this was not observed to be detrimental here. Overall, the present alloys achieve hardness values up to ∼600 HV, comparable to other age-hardened CoCrFeNi-based HEAs with Al and Ti additions [13,64]. It is worth noting that a significant increase in hardness is obtained with AR samples, even after extended ageing, showing the positive effect of pre-cold rolling in precipitation kinetics and strengthening.

In the present $(CoCrFeMnNi)_{100-x}(Al_2Ti)_x$ alloys, microstructural analysis by SEM and EBSD revealed significant σ and BCC precipitation after ageing. The increased hardness correlates directly with both the fraction and morphology of these precipitates, consistent with classical precipitation-strengthening mechanisms [1,65]. AR samples exhibit the highest hardness after ageing, likely due to the combined effect of finer precipitates and residual strains from rolling, which provides additional dislocation strengthening and accelerates precipitation. This is supported by the higher hardness with lower ageing temperature, where limited recovery and recrystallization preserve stored strain energy. Additionally, hardness decreases at longer ageing time, especially at higher ageing temperature, due to the coarsening of the precipitates. Conversely, ST samples show a very low initial hardness due to a soft, recrystallized FCC matrix, hardening progressively with ageing as σ and BCC precipitates form.

5. Conclusion

The effect of Al and Ti additions to CoCrFeMnNi on precipitation hardening has been assessed in this work. Three Al and Ti contents, $(CoCrFeMnNi)_{100-x}(Al_2Ti)_x$, $x = 6, 8, 10$, as well as three ageing temperatures, 650, 750, and 850 °C, with up to 160 h of ageing were investigated. Moreover, the effect of pre-cold rolling on the precipitation kinetics has been studied. Complex microstructures were obtained consisting of a FCC matrix with BCC and σ precipitates. The following conclusions can be drawn:

1. It has been identified that during ageing, first, a BCC second phase precipitates, second, a concurrent σ and BCC precipitations at FCC grain boundaries occurs, and third, needle-like BCC precipitates form inside FCC grains.
2. A higher Al/Ti content increases the volume fraction of secondary phases, increasing hardness. In the case of solution treated alloys, a hardness of 450 HV is reached after 24 h at 650 °C. In the case of pre-cold rolled alloys, a hardness of 600 HV is obtained after 2 h at 650 °C.
3. $L1_2$ precipitates have not been directly observed in any of the alloys in the range of heat treatments investigated in this work. In the case of Al_2Ti-6 aged at 650 °C, STEM-EDS characterization revealed two fine BCC precipitates in the FCC matrix. The first kind is rich in Al, Co, and Ni and its structure is ordered $L2_1$. The second kind is rich in Cr and is disordered A2.

Overall, this study shows that PH in (Al_2Ti)-containing CoCrFeMnNi HEAs is dominated by the formation of σ and BCC phases rather than $L1_2$. While the present work demonstrates significant hardness improvements, future investigations should address the influence of the precipitates on other properties, especially tensile behaviour, to balance strength and ductility. The high hardness and thermal stability of these microstructures make such alloys potential candidates for wear-resistant coatings.

CRediT authorship contribution statement

Antoine Hilhorst: Writing – review & editing, Writing – original draft, Visualization, Project administration, Methodology, Investigation, Formal analysis, Data curation, Conceptualization. **Alvise Miotti Bettanini:** Methodology, Investigation. **Mike Callahan:** Methodology, Investigation. **Pascal J. Jacques:** Writing – review & editing, Supervision, Project administration, Funding acquisition, Conceptualization.

Declaration of competing interest

The authors declare that they have no known competing financial interests or personal relationships that could have appeared to influence the work reported in this paper.

Acknowledgements

The authors would like to thank A. Béché for helping with the TEM characterization and analysis as well as for fruitful discussion of the present work. The research was funded by the Walloon Region under the agreement No. 1610154-EntroTough in the context of the 2016 WallInnov call. AH acknowledges financial support through F.R.S.FNRS chargé de recherche mandate (ID 40016846). This work was supported by the FNRS under Grant GEQ (Large Equipment) – UG01622F. This work has been performed with the help of the Lacami technological platform of UCLouvain.

Appendix A. Supplementary data

Supplementary material related to this article can be found online at https://doi.org/10.1016/j.jallcom.2025.185757.

Data availability

The data that support the findings of this study are available from the corresponding author upon reasonable request.

References

[1] T. Gladman, Precipitation hardening in metals, Mater. Sci. Technol. 15 (1) (1999) 30–36.
[2] Boxuan Cao, Tao Yang, Wei hong Liu, C.T. Liu, Precipitation-hardened high-entropy alloys for high-temperature applications: A critical review, MRS Bull. 44 (11) (2019) 854–859.
[3] Hamed Shahmir, Mohammad Sajad Mehranpour, Seyed Amir Arsalan Shams, Terence G. Langdon, Twenty years of the CoCrFeNiMn high-entropy alloy: Achieving exceptional mechanical properties through microstructure engineering, J. Mater. Res. Technol. 23 (2023) 3362–3423.
[4] Bernd Gludovatz, Anton Hohenwarter, Dhiraj Catoor, Edwin H. Chang, Easo P. George, Robert O. Ritchie, A fracture-resistant high-entropy alloy for cryogenic applications, Science 345 (6201) (2014) 1153–1158.
[5] G. Laplanche, A. Kostka, C. Reinhart, J. Hunfeld, G. Eggeler, E.P. George, Reasons for the superior mechanical properties of medium-entropy CrCoNi compared to high-entropy CrMnFeCoNi, Acta Mater. 128 (2017) 292–303.
[6] Deep Choudhuri, Bharat Gwalani, Stephane Gorsse, Mageshwari Komarasamy, Srinivas A. Mantri, Srivilliputhur G. Srinivasan, Rajiv S. Mishra, Rajarshi Banerjee, Enhancing strength and strain hardenability via deformation twinning in fcc-based high entropy alloys reinforced with intermetallic compounds, Acta Mater. 165 (2019) 420–430.
[7] Yung-Ta Chen, Yao-Jen Chang, Hideyuki Murakami, Stéphane Gorsse, An-Chou Yeh, Designing high entropy superalloys for elevated temperature application, Scr. Mater. 187 (2020) 177–182.
[8] Kaimiao Liu, Mageshwari Komarasamy, Bharat Gwalani, Shivakant Shukla, Rajiv S. Mishra, Fatigue behavior of ultrafine grained triplex Al0.3CoCrFeNi high entropy alloy, Scr. Mater. 158 (2019) 116–120.
[9] X.S. Liu, R. Li, A.X. Li, S. Xu, H. Yang, S.B. Yu, M.H. Jiang, C. Huo, P.F. Yu, Y.Y. Wang, G. Li, A novel high-strength and high-ductility CoCrNi medium entropy alloy by Ti/Mo co-doping, Mater. Lett. 326 (2022) 132929.
[10] M.V. Klimova, D.G. Shaysultanov, S.V. Zherebtsov, N.D. Stepanov, Effect of second phase particles on mechanical properties and grain growth in a CoCrFeMnNi high entropy alloy, Mater. Sci. Eng.: A 748 (2019) 228–235.
[11] Jeong Min Park, Jongun Moon, Jae Wung Bae, Dong Hyuk Kim, Yong Hee Jo, Sunghak Lee, Hyoung Seop Kim, Role of BCC phase on tensile behavior of dual-phase Al0.5CoCrFeMnNi high-entropy alloy at cryogenic temperature, Mater. Sci. Eng.: A 746 (2019) 443–447.
[12] Mohammad Sajad Mehranpour, Hamed Shahmir, Alireza Derakhshandeh, Mahmoud Nili-Ahmadabadi, Significance of Ti addition on precipitation in CoCrFeNiMn high-entropy alloy, J. Alloy. Compd. 888 (2021) 161530.
[13] L. Gerdt, M. Müller, M. Heidowitzsch, J. Kaspar, E. Lopez, M. Zimmermann, C. Leyens, A. Hilhorst, P.J. Jacques, Alloy design of feedstock material for additive manufacturing—Exploring the Al-Co-Cr-Fe-Ni-Ti compositionally complex alloys, in: ITSC 2023, Québec City, Canada, 2023, pp. 414–421.

[14] W.H. Liu, Z.P. Lu, J.Y. He, J.H. Luan, Z.J. Wang, B. Liu, Yong Liu, M.W. Chen, C.T. Liu, Ductile CoCrFeNiMox high entropy alloys strengthened by hard intermetallic phases, Acta Mater. 116 (2016) 332–342.
[15] J.Y. He, H. Wang, Y. Wu, X.J. Liu, T.G. Nieh, Z.P. Lu, High-temperature plastic flow of a precipitation-hardened FeCoNiCr high entropy alloy, Mater. Sci. Eng.: A 686 (2017) 34–40.
[16] Tao Yang, Yilu Zhao, Weihong Liu, Jijung Kai, Chaintsuan Liu, $L1_2$ -strengthened high-entropy alloys for advanced structural applications, J. Mater. Res. 33 (19) (2018) 2983–2997.
[17] Lu Zhang, Yang Zhou, Xi Jin, Xingyu Du, Bangsheng Li, Precipitation-hardened high entropy alloys with excellent tensile properties, Mater. Sci. Eng.: A 732 (2018) 186–191.
[18] J. Kaspar, A. Hilhorst, L. Gerdt, M. Müller, M. Heidowitzsch, M. Kuczyk, A.M. Bettanini, P.J. Jacques, M. Zimmermann, C. Leyens, Combinatorial alloy design and microstructure evolution in laser-cladded Al–Co–Cr–Fe–Ni–Ti compositionally complex alloys, High Entropy Alloy. Mater. 1 (2) (2023) 361–378.
[19] J.Y. He, W.H. Liu, H. Wang, Y. Wu, X.J. Liu, T.G. Nieh, Z.P. Lu, Effects of Al addition on structural evolution and tensile properties of the FeCoNiCrMn high-entropy alloy system, Acta Mater. 62 (2014) 105–113.
[20] Y.Y. Zhao, H.W. Chen, Z.P. Lu, T.G. Nieh, Thermal stability and coarsening of coherent particles in a precipitation-hardened (NiCoFeCr)94Ti2Al4 high-entropy alloy, Acta Mater. 147 (2018) 184–194.
[21] T. Rieger, J.-M. Joubert, M. Laurent-Brocq, L. Perrière, I. Guillot, J.-P. Couzinié, Study of the FCC+L12 two-phase region in complex concentrated alloys based on the Al–Co–Cr–Fe–Ni–Ti system, Materialia 14 (2020) 100905.
[22] J. Joseph, M. Senadeera, Q. Chao, K.F. Shamlaye, S. Rana, S. Gupta, S. Venkatesh, P. Hodgson, M. Barnett, D. Fabijanic, Computational design of thermally stable and precipitation-hardened Al-Co-Cr-Fe-Ni-Ti high entropy alloys, J. Alloys Compd. 888 (2021) 161496.
[23] N. Choi, K.R. Lim, Y.S. Na, U. Glatzel, J.H. Park, Characterization of non-metallic inclusions and their influence on the mechanical properties of a FCC single-phase high-entropy alloy, J. Alloys Compd. 763 (2018) 546–557.
[24] X. Zuo, A. Miotti Bettanini, A. Hilhorst, P.J. Jacques, Influence of 5 at.%Al-Additions on the FCC to BCC phase transformation in CrFeNi concentrated alloys, J. Phase Equilibria Diffus. 42 (5) (2021) 794–813.
[25] Linfei Xia, Qingfeng Wu, Kexuan Zhou, Bin Han, Feng He, Zhijun Wang, Concurrent recrystallization and precipitation for combination of superior precipitation and grain boundary hardening in Co37Cr20Ni37Ti3Al3 high-entropy alloy, Met. Mater. Int. 28 (12) (2022) 2863–2873.
[26] J.Y. He, H. Wang, Y. Wu, X.J. Liu, H.H. Mao, T.G. Nieh, Z.P. Lu, Precipitation behavior and its effects on tensile properties of FeCoNiCr high-entropy alloys, Intermetallics 79 (2016) 41–52.
[27] Min-Gu Jo, Jin-Yoo Suh, Myung-Yeon Kim, Han-Jin Kim, Woo-Sang Jung, Dong-Ik Kim, Heung Nam Han, High temperature tensile and creep properties of CrMnFeCoNi and CrFeCoNi high-entropy alloys, Mater. Sci. Eng.: A 838 (2022) 142748.
[28] Hamed Shahmir, Mahmoud Nili-Ahmadabadi, Ahad Shafiee, Terence G. Langdon, Effect of a minor titanium addition on the superplastic properties of a CoCrFeNiMn high-entropy alloy processed by high-pressure torsion, Mater. Sci. Eng.: A 718 (2018) 468–476.
[29] Yao-Jen Chang, An-Chou Yeh, The evolution of microstructures and high temperature properties of AlxCo1.5CrFeNi1.5Tiy high entropy alloys, J. Alloys Compd. 653 (2015) 379–385.
[30] H.M. Daoud, A.M. Manzoni, N. Wanderka, U. Glatzel, High-temperature tensile strength of Al10Co25Cr8Fe15Ni36Ti6 compositionally complex alloy (high-entropy alloy), J. Oper. Manage. 67 (10) (2015) 2271–2277.
[31] Takuro Masumura, Tatsuya Honda, Kosuke Naridomi, Shohei Uranaka, Toshihiro Tsuchiyama, Goro Miyamoto, Shota Yamasaki, Age-hardening behavior in high-nitrogen stable austenitic stainless steel, Mater. Trans. 63 (2) (2022) 163–169.
[32] Wojciech Polkowski, Adelajda Polkowska, Sebastian Lech, Aging behavior of Haynes® 282® wrought nickel superalloy subjected to a cold pre-deformation by differential speed rolling, J. Alloys Compd. 860 (2021) 158418.
[33] Vickey Nandal, R. Sarvesha, Sudhanshu S. Singh, E-Wen Huang, Yao-Jen Chang, An-Chou Yeh, Suresh Neelakantan, Jayant Jain, Influence of pre-deformation on the precipitation characteristics of aged non-equiatomic Co1.5CrFeNi1.5 high entropy alloys with Ti and Al additions, J. Alloys Compd. 855 (2021) 157521.
[34] Bo Li, Kaisheng Ming, Kang Tu, Zonglin Li, Lichen Bai, Shijian Zheng, Combined strengthening from nanoprecipitates, stacking faults and nano-twins enables a strong and ductile medium-entropy alloy, Mater. Sci. Eng.: A (2023) 145828.
[35] Yong Zhao, Mingliang Wang, Hongzhi Cui, Yuqiao Zhao, Xiaojie Song, Yong Zeng, Xiaohua Gao, Feng Lu, Canming Wang, Qiang Song, Effects of Ti-to-Al ratios on the phases, microstructures, mechanical properties, and corrosion resistance of Al2-xCoCrFeNiTix high-entropy alloys, J. Alloy. Compd. 805 (2019) 585–596.
[36] J.-O. Andersson, Thomas Helander, Lars Höglund, Pingfang Shi, Bo Sundman, Thermo-Calc & DICTRA, computational tools for materials science, Calphad 26 (2) (2002) 273–312.
[37] X.-F. Gu, T. Furuhara, W.-Z. Zhang, PTCLab : Free and open-source software for calculating phase transformation crystallography, J. Appl. Crystallogr. 49 (3) (2016) 1099–1106.
[38] D. Kiener, C. Motz, M. Rester, M. Jenko, G. Dehm, FIB damage of Cu and possible consequences for miniaturized mechanical tests, Mater. Sci. Eng.: A 459 (1–2) (2007) 262–272.
[39] Frederik Otto, Antonín Dlouhỳ, Konda Gokuldoss Pradeep, Monika Kuběnová, Dierk Raabe, G. Eggeler, Easo P. George, Decomposition of the single-phase high-entropy alloy CrMnFeCoNi after prolonged anneals at intermediate temperatures, Acta Mater. 112 (2016) 40–52.
[40] Jongtae Kim, Soon Jik Hong, Jin Kyu Lee, Ki Buem Kim, Jong Hyeon Lee, Junhee Han, Chanho Lee, Gian Song, Development of coherent-precipitate-hardened high-entropy alloys with hierarchical NiAl/Ni2TiAl precipitates in CrMnFeCoNiAlxTiy alloys, Mater. Sci. Eng.: A 823 (2021) 141763.
[41] Shih-Hsien Chang, In situ TEM observation of $\Gamma\prime$, γ'' and δ precipitations on Inconel 718 superalloy through HIP treatment, J. Alloys Compd. 486 (1–2) (2009) 716–721.
[42] S. Dasari, A. Sarkar, A. Sharma, B. Gwalani, D. Choudhuri, V. Soni, S. Manda, I. Samajdar, R. Banerjee, Recovery of cold-worked Al0.3CoCrFeNi complex concentrated alloy through twinning assisted B2 precipitation, Acta Mater. 202 (2021) 448–462.
[43] Jian Peng, Zi yong Li, Xin bo Ji, Yan le Sun, Li ming Fu, Ai dang Shan, Decomposition kinetics of carbon-doped FeCoCrNiMn high-entropy alloy at intermediate temperature, Trans. Nonferr. Met. Soc. China 30 (7) (2020) 1884–1894.
[44] Juliusz Dabrowa, Marek Danielewski, State-of-the-art diffusion studies in the high entropy alloys, Metals 10 (3) (2020) 347.
[45] Tumpa R. Paul, Irina V. Belova, Graeme E. Murch, Analysis of diffusion in high entropy alloys, Mater. Chem. Phys. 210 (2018) 301–308.
[46] Sriswaroop Dasari, Abhishek Sharma, Stéphane Gorsse, Advika Chesetti, Rajarshi Banerjee, Non-classical nucleation of ordered L12 precipitates in the FCC based Al0.25CoFeNi high entropy alloy, J. Appl. Phys. 134 (1) (2023) 015102.
[47] L. Gerdt, A. Hilhorst, M. Müller, M. Heidowitzsch, J. Kaspar, E. Lopez, M. Zimmermann, P.J. Jacques, Tuning the microstructure and mechanical properties of Al-Co-Cr-Fe-Ni-Ti compositionally complex alloys manufactured by means of L-DED, J. Therm. Spray Technol. (2024).
[48] Jiacheng Niu, Zhiqiang Fu, Weiping Chen, Chenliang Chu, Dezhi Zhu, Haiming Wen, Influence of partial substitution of Cr by Al on microstructure and mechanical behavior of Fe30Ni35Cr35 multi-principal element alloy, Vacuum 215 (2023) 112282.
[49] Jingqian Chen, Yongkang Zhou, Lili Yu, Shuai Zeng, Aiming Wang, Huameng Fu, Hongwei Zhang, Haifeng Zhang, Zhengwang Zhu, Enhancing strength-ductility combination of Fe–Ni–Cr–Al–Ti high-entropy alloys via co-precipitation of sigma and L21 phases, Mater. Sci. Eng.: A 913 (2024) 147062.
[50] Guanghui Yang, Jiyeon Kang, Jin-Kyung Kim, Joo Hyun Park, Enhanced strength-ductility balance of the (CoCrFeNiMn)95.2Al3.2Ti1.6 high-entropy alloy by co-precipitation of the B2 and sigma phases, Mater. Sci. Eng.: A 873 (2023) 145039.
[51] J. Joseph, M. Annasamy, S.R. Kada, P.D. Hodgson, M.R. Barnett, D.M. Fabijanic, Optimising the Al and Ti compositional window for the design of γ' (L12)-strengthened Al–Co–Cr–Fe–Ni–Ti high entropy alloys, Mater. Sci. Eng.: A 835 (2022) 142620.
[52] Shengzhi Li, Qingsong Shu, Xiaocen Ding, Yao Lu, Hongyuan Wen, Jiashi Zhou, Lanting Zhang, Bingbing Zhao, An order–disorder phase transition in alloy 783 bolts after long-term service, Scr. Mater. 243 (2024) 115983.
[53] André Pineau, Amine A. Benzerga, Thomas Pardoen, Failure of metals I: Brittle and ductile fracture, Acta Mater. 107 (2016) 424–483.
[54] Hyojin Park, Qingfeng Wu, Yoon-Uk Heo, Sun Ig Hong, Rae Eon Kim, Do Won Lee, Soung Yeoul Ahn, Zhe Gao, Jae Heung Lee, Hyo Moon Joo, Jongun Moon, Young-Sang Na, Jae il Jang, Hyoung Seop Kim, Manipulating grain boundary migration to fabricate integral core–shell structure with enhanced strain hardening in Ni-based high-entropy alloy, J. Mater. Sci. Technol. 242 (2026) 213–225.
[55] Rae Eon Kim, Jae Heung Lee, Farahnaz Haftlang, Sang-Ho Oh, Byeong-Joo Lee, Qingfeng Wu, Yoon-Uk Heo, Hyoung Seop Kim, Hierarchical ferrous medium entropy with heterogeneous precipitates embedded in core–shell grain structure for superior mechanical properties, Acta Mater. 281 (2024) 120397.
[56] Chih-Chun Hsieh, Weite Wu, Overview of intermetallic sigma phase precipitation in stainless steels, Int. Sch. Res. Not. (2012) 2012.
[57] R.C. Reed, M.P. Jackson, Y.S. Na, Characterization and modeling of the precipitation of the sigma phase in UDIMET 720 and UDIMET 720LI, Met. Mater. Trans. A 30 (3) (1999) 521–533.
[58] Antoine Hilhorst, P.J. Jacques, Diffusion multiples as a tool to efficiently explore the composition space of high entropy alloys, J. Phase Equilibria Diffus. (2021) 1–12.
[59] G. Laplanche, S. Berglund, C. Reinhart, A. Kostka, F. Fox, E.P. George, Phase stability and kinetics of σ-phase precipitation in CrMnFeCoNi high-entropy alloys, Acta Mater. 161 (2018) 338–351.
[60] Wenjun Lu, Wenqi Guo, Zhangwei Wang, Jianjun Li, Fengchao An, Gerhard Dehm, Dierk Raabe, Christian H. Liebscher, Zhiming Li, Advancing strength and counteracting embrittlement by displacive transformation in heterogeneous high-entropy alloys containing sigma phase, Acta Mater. 246 (2023) 118717.

[61] Ken Cho, Yumi Fujioka, Takeshi Nagase, Hiroyuki Y. Yasuda, Grain refinement of non-equiatomic Cr-rich CoCrFeMnNi high-entropy alloys through combination of cold rolling and precipitation of σ phase, Mater. Sci. Eng.: A 735 (2018) 191–200.

[62] G. Laplanche, U.F. Volkert, G. Eggeler, E.P. George, Oxidation behavior of the CrMnFeCoNi high-entropy alloy, Oxid. Met. 85 (5–6) (2016) 629–645.

[63] Jong Woo Won, Minju Kang, Heoun-Jun Kwon, Ka Ram Lim, Seong Moon Seo, Young Sang Na, Edge-cracking behavior of CoCrFeMnNi high-entropy alloy during hot rolling, Met. Mater. Int. 24 (6) (2018) 1432–1437.

[64] Vickey Nandal, R. Sarvesha, Sudhanshu S. Singh, E-Wen Huang, Yao-Jen Chang, An-Chou Yeh, Jayant Jain, Suresh Neelakantan, Enhanced age hardening effects in FCC based Co1.5CrFeNi1.5 high entropy alloys with varying Ti and Al contents, Materialia 13 (2020) 100823.

[65] Erhard Hornbogen, Hundred years of precipitation hardening, J. Light. Met. 1 (2) (2001) 127–132.